Journal of Materials Chemistry C

PAPER

View Article Online
View Journal | View Issue

Cite this: J. Mater. Chem. C, 2014, 2, 8142

ZnO anchored graphene hydrophobic nanocomposite-based bulk heterojunction solar cells showing enhanced short-circuit current†

Rajni Sharma,[a] Firoz Alam,[b] A. K. Sharma,[c] V. Dutta[b] and S. K. Dhawan*[a]

Received 21st May 2014
Accepted 30th July 2014

DOI: 10.1039/c4tc01056f

www.rsc.org/MaterialsC

Hydrophobic and surfactant-free ZnO nanoparticles and ZnO decorated graphene nanocomposite (Z@G) with narrow and uniform size distribution were synthesized by a time-efficient microwave-assisted hydrothermal reaction that can be used specifically for application in hybrid photovoltaics. The synthesized ZnO nanoparticles and Z@G nanocomposite showed stable and clear dispersion in chloroform and methanol (with volume ratio of 9 : 1) and chloroform and ethanol (volume ratio 9 : 1). Being hydrophobic, these inorganic samples blend very well with organic polymer solution in chlorobenzene, which is a prerequisite to cast smooth and undisrupted film for hybrid solar cell application. The introduction of these hydrophobic nanoparticles into PCPDTBT:PCBM-based bulk-heterojunction polymer solar cells resulted in significant improvement in solar cell J–V characteristics with enhancement in open circuit voltage (V_{OC}), short circuit current density (J_{SC}) and thereby overall improvement in cell efficiency. With the optimization of the weight ratio of polymer, fullerene and synthesized ZnO nanoparticles/Z@G nanocomposite, the power conversion efficiencies 1.76% and 3.65% were achieved.

Introduction

In order to compensate for the continuous depleting stock of nonrenewable energy resources and fulfil the emerging demand of green energy, the exploitation of solar energy *via* the photovoltaic (PV) technology is one of the most appealing solutions. Despite the high power conversion efficiency, the higher maintenance cost and expensive processing technology used in inorganic PV (silicon-based solar cells) has enforced the thinking about other cost-effective PV technology alternatives. Organic PV (conjugated polymer-based organic solar cells) has succeeded in drawing the attention of researchers worldwide as being viable, low-cost fabrication technology, which is highly versatile in terms of chemical structure, *i.e.* advanced organic chemistry, large area synthesis and, most importantly, eco-friendly nature. In addition to the numerous favourable properties that may begin an era of low-cost PV, organic PV is now facing significant challenges for developing highly efficient polymer-based devices because of the bulk recombination losses and low carrier diffusion length, causing less efficient charge separation and transport to respective electrodes,[1–6] as well as limitations in the device architecture.

Because of the low dielectric constant value (2 to 3),[7] the absorption of photons by conjugated polymers gives rise to the generation of strongly bound electron and hole pairs (*i.e.* exciton with the binding energy ~400 meV) instead of the free charge carriers as in the case of inorganic semiconductors.[8] Hence, in organic polymers, a strong field is required to dissociate strongly bound excitons into free electrons and holes.[9] The low exciton diffusion length (10–15 nm) or short lifetime (hundreds of picoseconds)[10] is also of major concern that ultimately contributes to the recombination losses and therefore low photocurrent generation and low power conversion efficiency. Moreover, the low charge carrier mobility (10^{-7} to 1 cm^2 V^{-1} s^{-1}) in organic polymers hinders the efficient charge transportation toward respective electrodes and increases the recombination losses. As per the literature,[11–14] most of the polymer solar cells have been reported using conjugated polymers as donor and organic fullerenes as acceptor. The fullerenes act as efficient absorbers, but at the same time, they do not contribute to the absorption, as they are non-photoactive in nature.[15] This has led to the thinking that exploiting the properties of nanostructured inorganic semiconducting materials in polymer solar cells as an acceptor may be better and to the evolution of organic–inorganic hybrid solar cells. The inorganic semiconductors contribute towards elevated photocurrent generation by the way of an improved

[a]CSIR-National Physical Laboratory, Dr K. S. Krishnan Marg, New Delhi-110012, India. E-mail: skdhawan@mail.nplindia.ernet.in; Fax: +91-11-25726938; Tel: +91-11-45609401

[b]Photovoltaic Laboratory, Centre for Energy Studies, Indian Institute of Technology Delhi, Hauz Khas, New Delhi 110016, India

[c]National Centre for Photovoltaic Research and Education (NCPRE), Department of Electrical Engineering, IIT-Bombay, Powai, Mumbai-470006, India

† Electronic supplementary information (ESI) available. See DOI: 10.1039/c4tc01056f

solar spectrum absorption with tuneability of the band gap and better charge collection and transportation *via* high charge carrier mobility, long life time or significant diffusion length.

Zinc oxide (ZnO) qualifies as a most promising inorganic semiconductor towards optoelectronic applications with its numerous useful properties, like wide band gap (3.32 eV for bulk)[16] that can be easily tuned by growing its nanostructures with varying morphologies, low crystallization temperature, high chemical stability, good charge carrier mobility (to overcome charge transport limitations in organic–inorganic hybrid solar cells),[17–19] piezoelectric nature (enhance photocurrent generation and solar to electric power conversion owing to electric field associated with polarisation induced by acoustic vibrations),[20] abundance in the earth's crust, cheap synthesis and non-toxic nature.[21]

Another potential material class is carbonaceous materials, which find applications in various optoelectronic devices because of their attracting properties like their existence in a variety of nanostructures (CNTs or graphene), noteworthy electrical and thermal performance parameters, and abundant and eco-friendly nature.[22,23] Lots of work has already been conducted on CNTs, even regarding their application in PV, but not much has happened specifically for advancement in terms of efficiency and decrement in terms of cost. Graphene with its large surface area (2600 $m^2 g^{-1}$),[24] high carrier mobility (200 000 $cm^2 V^{-1} s^{-1}$),[25] excellent thermal conductivity (5000 W $m^{-1} K^{-1}$),[26] tuneable band gap (0 to 250 meV),[27] and fine electron acceptor, is extremely important and even less expensive when synthesized on a large scale in comparison to CNTs.[28,29] Graphene sheets generally restack and form agglomerates when used as such owing to van der Waals interaction. To solve this problem, either a surfactant can be used or the graphene can be anchored by nanoparticles. The use of surfactants is usually not favoured in solar cell applications as they hinder the charge transport, resulting in poor device performance. The 2D structure of graphene provides a scaffold to anchor metallic and semiconducting nanoparticles and thus to develop various hybrid assemblies.[30] Graphene's capability to interact with the excited states of semiconducting nanoparticles and undergo charge transfer by monitoring the emission life time of ZnO nanoparticles–graphene (inorganic–organic) composite-based samples is already reported in the literature.[31] The crystal structure of graphene is 2D hexagonal and ZnO exists in hexagonal wurtzite form; thus, there is very good lattice compatibility between the two.[32] Specifically, it is ZnO that absorbs photons and generates photoelectrons, whereas graphene only helps in the conduction of these electrons. Moreover, improvement in charge transfer in Z@G nanocomposite rather than pure ZnO has already been reported.[33] This effective electron transfer from ZnO nanoparticles to graphene lowers the recombination of charge carrier, which ultimately improves the solar cell performance.

A microwave-assisted hydrothermal route is a prime choice for the synthesis of ZnO nanoparticles and graphene-based composites as it affords time effectiveness in a one-step reaction (reaction time can be shortened by adjusting the power, pressure and temperature of the reaction) and yields uniform morphology, *i.e.* small sized particles with a narrow size distribution.[34,35] Moreover, for the successful synthesis of ZnO–graphene (Z@G) nanocomposite, an effective interfacing between ZnO nanoparticles and graphene sheets without deteriorating their properties is vital. Therefore, a hydrothermal route is preferred for preserving the structural and electrical properties of the individual components.[36]

Already a lot of work has been performed on ZnO-based devices where many researchers replaced fullerenes completely by ZnO (synthesized *ex situ* or *in situ*, rod shaped or tetra-pod) as an electron acceptor without considerable significant results being obtained.[37,38] Moreover, ZnO–graphene has been used as an electron acceptor with P3HT[39] reporting the PCE of 0.98% and also as a buffer layer in an inverted solar cell[33] with an enhanced efficiency of 4.15%. The novelty of our work lies on the surfactant-free synthesis of hydrophobic ZnO nanoparticles (and ZnO–graphene nanocomposite) for better charge transportation in polymer solar cells. The hydrophobic nature (soluble and stable in non-polar solvents like chloroform and chlorobenzene) of ZnO nanoparticles helps in the casting of a smooth and continuous film for hybrid solar cell application. After the successful synthesis of ZnO nanoparticles, ZnO–graphene (Z@G) nanocomposite is also worked upon using reduced graphene oxide (RGO) as a precursor. The microwave-assisted route is very significant for the reduction of RGO. Moreover, the hydrophobic nature of both ZnO and graphene does not require any modification on the graphene surface (*via* surfactants) to anchor ZnO nanoparticles over the graphene sheet.[40] We can then use these ZnO nanoparticles and Z@G nanocomposite to fabricate a hybrid solar cell. Both graphene and PCBM are different forms of carbon; thus, they are expected to form hybrids that may further improve charge conduction. Therefore, instead of using these nanoparticles or nanocomposites as a replacement, we use them as a supplement in PCPDTBT:PCBM-based conventional type (non-inverted) solar cells.

Experimental procedure

The chemicals used in the synthesis of ZnO nanoparticles and ZnO decorated graphene nanocomposites are zinc acetate dihydrate, potassium hydroxide, methanol from Merck, India, and RGO was procured from ACS Materials. A Monowave 300 (Anton Paar) microwave reactor was used for the above-mentioned synthesis of nanoparticles and nanocomposite.

Synthesis of hydrophobic ZnO nanoparticles

Zinc acetate (0.6 g) was dissolved in 20 ml of methanol and 10 ml of distilled water at 60 °C. Then, a solution of 0.3 g of potassium hydroxide in 13 ml of methanol was added and stirred for 10–15 minutes to obtain a clear solution. 25 ml of the final solution was poured into a 30 ml glass tube tightened with septum, and finally placed in a Teflon-lined microwave reactor. The reaction was carried out at 160 °C for half an hour, and then the reactor was cooled down to 55 °C to obtain a milky white solution. The solution was left untouched for 10 minutes to

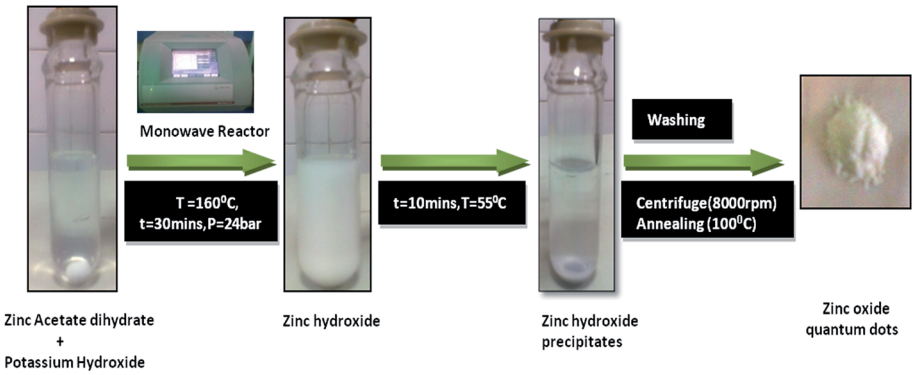

Fig. 1 The ZnO nanoparticle synthesis process flow.

allow the precipitates to settle down. The obtained precipitates were washed and centrifuged for 3–4 times at 8000 rpm, followed by annealing at 100 °C for half an hour to obtain pure ZnO nanoparticles. The process steps captured at various stages are also shown in Fig. 1. Moreover, the variation of pressure, temperature and power during the reaction has been given as S1 in ESI along with hydrophobic evaluation as S3.† The clear and stable dispersion of ZnO nanoparticles was obtained in the mixture of chloroform and methanol (with volume ratio 9 : 1).

Synthesis of ZnO nanoparticles decorated graphene (or Z@G) nanocomposite

ZnO nanoparticles decorated graphene was synthesized by the hydrothermal reaction in a microwave reactor. A solution of RGO in ethanol was prepared by adding 5 mg of commercial RGO (ACS materials) in 10 ml of ethanol and ultrasonication for 10–15 minutes. In a separate beaker, another solution was prepared by dissolving 0.6 g of zinc acetate dehydrate in 20 ml of methanol and 10 ml distilled water at 60 °C, followed by the addition of 0.3 g of KOH dissolved in 13 ml of methanol with stirring for 10–15 minutes. The RGO solution was added to the zinc precursor and again ultrasonicated for 10 minutes. 25 ml of the final solution was poured into a glass tube with a total capacity of 30 ml and was tightened with septum and placed in a Teflon-lined reactor. The reaction was carried out at 160 °C for an hour and finally cooled down to 55 °C. After the completion of the reaction, the greyish colour precipitates obtained were washed and centrifuged 3–4 times at 10 000 rpm and finally annealed at 100 °C for half an hour to obtain ZnO decorated graphene nanocomposite (Z@G). Fig. 2 illustrates the process steps for preparing the ZnO decorated graphene nanocomposite. The graph showing variation of temperature, pressure and power during reaction is shown as S2 in ESI.† The stable suspension was obtained in a mixture of chloroform and ethanol (with volume ratio 9 : 1).

Characterization of ZnO nanoparticles and ZnO decorated graphene (Z@G) nanocomposite

In order to investigate the particle size and microstructural properties of the synthesized ZnO nanoparticles and Z@G nanocomposite, transmission electron microscopy (TEM) and high-resolution transmission electron microscopy (HRTEM) measurements were performed using the Tecnai G2 F30 S-Twin instrument operating at 300 kV as accelerating voltage using a drop cast sample dispersed in chloroform onto a carbon coated copper grid. The Shimadzu UV-1601 spectrophotometer was used to record absorption spectra. Photoluminescence spectra were acquired using Perkin Elmer LF55 having a xenon source spectrophotometer (in the wavelength region of 320–500 nm). Atomic force microscopy (AFM) studies were performed by multimode AFM with Nanoscope V controller (Veeco, USA) in tapping mode. Fourier transform infrared analysis (FTIR) was carried out using Nicolet 5700 in transmission mode in the wavenumber range of 400–4000 cm^{-1} to determine the functional groups present in the synthesized samples. Crystal structure and phase analysis was performed by using D8-Advance XRD (Bruker) using Cu Kα radiation (wavelength, λ = 1.54 Å) in the scattering range (2θ) of 10°–80° with a scan rate of 0.02° s^{-1} and a slit width of 0.1 mm. Raman scattering was performed by using Renishaw in Via Reflex spectrometer (UK) with an excitation source at 514.5 nm with a resolution less than 1.0 cm^{-1}. To calculate the hydrophobicity of synthesized ZnO nanoparticles, contact angles were recorded on the Drop Shape Analysis System DSA10MK2 from Krüss GmbH, Germany.

Hybrid solar cell fabrication and characterization

ZnO nanoparticles and ZnO-decorated graphene nanocomposite (Z@G)-based bulk heterojunction solar cells (ITO/PEDOT:PSS/PCPDTBT:PCBM:ZnO (or Z@G)/Al) with an active area of 0.1 cm^2 were fabricated by varying the concentration of PCPDTBT:PCBM:ZnO (or Z@G) and also by varying the weight ratio of the polymer, fullerene and nanoparticles. The solution of the polymer, fullerene and ZnO (or Z@G) in chlorobenzene was spin-coated as an active layer on the ITO-coated glass substrate of sheet resistance 10–14 Ω cm^{-1} with poly(ethylenedioxythiophene):poly(styrene sulfonic acid) (PEDOT:PSS) coating as the buffer layer. Here, ITO acts as the bottom electrode. PEDOT:PSS coating was performed at 2000 rpm, whereas the active layer was spin-coated at 800 rpm under ambient conditions. Finally, 100 nm thick aluminium (Al) was deposited

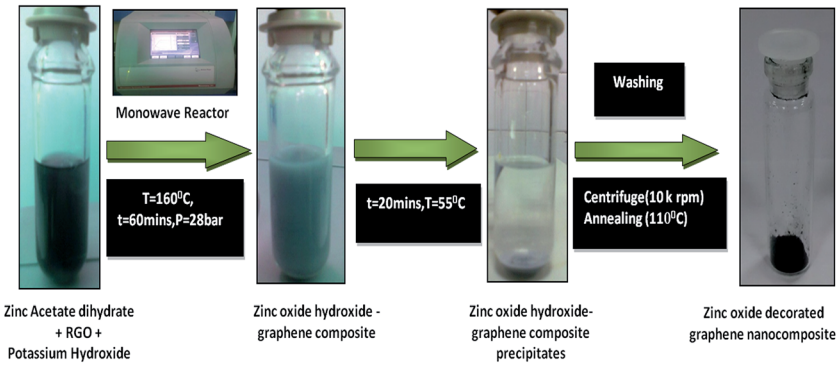

Fig. 2 The ZnO nanoparticles decorated graphene nanocomposite synthesis process flow.

by a thermal evaporation unit through a shadow mask at 2×10^{-6} Torr as the top metal contact of the device.

The performance of polymer bulk heterojunction solar cells fabricated with ZnO nanoparticles and ZnO-decorated graphene nanocomposite (Z@G) was evaluated with the current density–voltage (J–V) characteristics measured with a class AAA solar simulator (sol3A Oriel Newport USA) equipped with a xenon lamp used as a light source under standard test conditions (STC).

Results and discussion

Structural and morphological investigations

The XRD spectra for reduced graphene oxide (RGO), ZnO nanoparticles (ZnO) and ZnO–graphene nanocomposite (Z@G) are shown in Fig. 3 to analyze the phase and crystallinity of ZnO and RGO along with the interlayer effect in hybrid or composite. A broad band of a (002) peak of graphite at $2\theta = 29.37°$ is observed in RGO, which corresponds to the d-spacing of 0.31 nm. The reason for the small d value lies in aggregation of the reduced graphene sheets because of weak van der Waals force of attraction between nanosheets.[41] The XRD pattern of ZnO nanoparticles shows the reflections (100), (002), (101), (102), (110), (103), (112), (004) and (202) of ZnO in a hexagonal wurtzite lattice.[42] The absence of any secondary phase confirms the synthesis of pure and single phase ZnO nanoparticles. In addition, small-sized ZnO nanoparticles are directly evidenced from the broad peaks. The calculated average crystallite size using Scherrer's equation for the ZnO sample comes out to be 4.5 nm, whereas for the Z@G nanocomposite the evaluated crystallite size is around 8 nm. In the Z@G XRD pattern, no diffraction peak corresponding to RGO was observed. This can be explained in two ways: (i) lesser amount, giving relatively low diffraction intensity of RGO than ZnO in the Z@G nanocomposite, and (ii) the anchoring of ZnO nanoparticles on RGO may inhibit the restacking of carbon sheets, which results in a weak diffraction peak or no diffraction peak.[43,44]

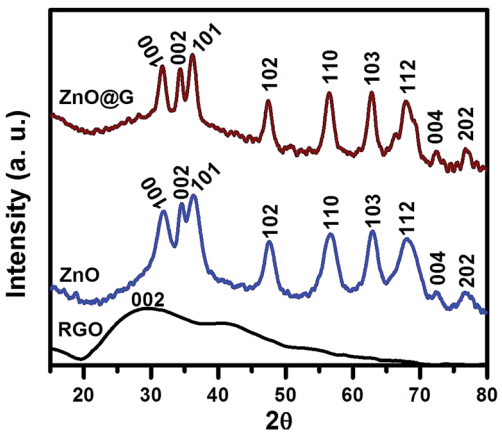

Fig. 3 The XRD intensities for reduced graphene oxide (RGO), ZnO nanoparticles (ZnO) and ZnO–graphene nanocomposite (Z@G) described phase and crystallinity of ZnO and RGO along with the interlayer effect in hybrid or the composite.

The morphological analysis of synthesized ZnO nanoparticles and Z@G nanocomposite heterostructure using high-resolution transmission electron microscopy (HRTEM) is given in Fig. 4. The HRTEM image of the ZnO sample shown in Fig. 4(a) clearly illustrates the quasi spherical ZnO nanoparticles in the range 4–8 nm with an average size of 5.25 nm as depicted in the histogram. Fig. 4(b) shows the image at higher resolution and a selected area electron diffraction (SAED) pattern in the inset. The SAED pattern provides a clear evidence of the highly crystalline ZnO structure with all diffraction rings being indexed to the hexagonal wurtzite phase of ZnO. This observation supports the synthesis of phase pure ZnO nanoparticles *via* the time-efficient hydrothermal method. The lattice fringes encircled image shown in Fig. 4(b) gives an interplanar distance of 0.28 nm, which can be assigned to the (100) plane of hexagonal ZnO. Fig. 4(c) illustrates the ZnO nanoparticles–graphene nanocomposite (Z@G) images having ZnO nanoparticles with nearly spherical symmetry and narrow size distribution in the range 3–11 nm anchored on the graphene sheet. The average size of ZnO nanoparticles decorated on graphene sheet is ~7 nm from the histogram. The enhancement in the average size of ZnO nanoparticles from 5.25 nm to 7 nm with the introduction of graphene is probably because of the longer duration of annealing time (30 min to 60 min) that results in the growth of ZnO nanoparticles. Moreover, close contact between ZnO nanoparticles and graphene can be

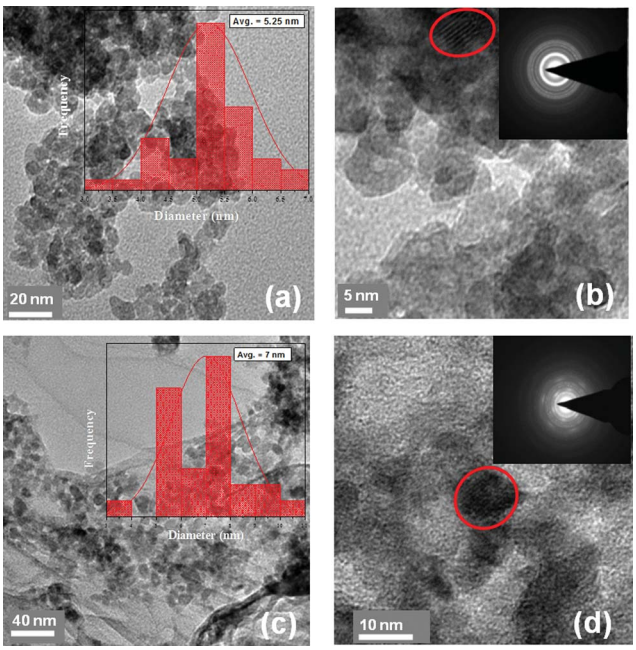

Fig. 4 The HRTEM image of (a) ZnO nanoparticles; and (c) ZnO–graphene nanocomposite (Z@G), with average particle size of 5.25 nm and 7 nm, respectively, as obtained from histogram shown in the inset; highly resolved images (b) and (d) with SAED pattern in the inset featuring highly crystalline ZnO structure indexed as hexagonal wurtzite phase and polycrystalline nature of Z@G nanocomposite, respectively.

witnessed from the HRTEM image shown in Fig. 4(c). This close contact will provide proper electronic interaction between graphene and ZnO nanoparticles that is very much required to have better charge separation (or less charge carrier recombination)[45] and is therefore crucial for improvement in the power conversion efficiency of hybrid solar cells. The high magnification image corresponding to Z@G nanocomposite, elaborated in SAED pattern taken for the encircled fringes, is shown in Fig. 4(d). The polycrystalline nature of the Z@G nanocomposite is evidenced from the SAED pattern.

Optical investigations

The absorption spectra of the synthesized ZnO nanoparticles and Z@G nanocomposite are shown in Fig. 5. It is clearly observed that in pure ZnO, a strong absorption peak at 364 nm, having a corresponding band gap of 3.4 eV, is at a lower wavelength (blue shifted) than that for bulk ZnO (corresponding to 3.32 eV) as per the literature.[16] This blue shift is due to the synthesis of small-sized ZnO nanoparticles *via* the facile and simple hydrothermal method. In addition, the sharp characteristic absorption peak clearly points to the good crystallinity and high purity of synthesized ZnO nanoparticles. The Z@G nanocomposite shows an absorption peak at 372 nm. The possible reason for this red shift may lie as follows: (1) the nanocomposite structure, which may favour the prominent absorption of ZnO rather than that of the graphene, (2) coupling between ZnO and graphene and (3) increased particle size in

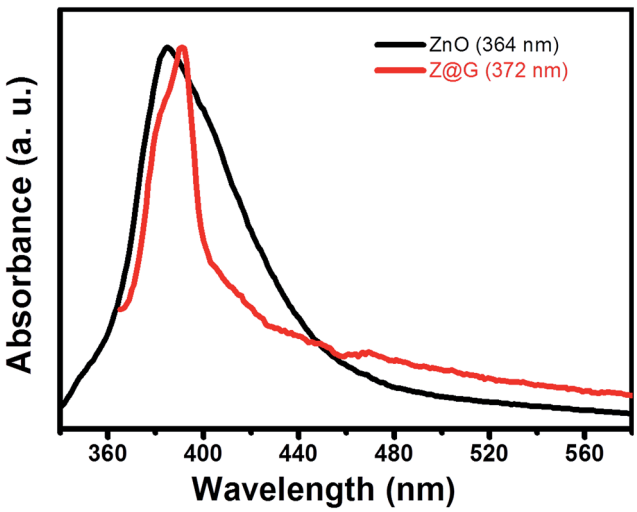

Fig. 5 The normalized UV-Vis spectra of synthesized ZnO nanoparticles and Z@G nanocomposite with strong absorption peaks at 364 nm and 372 nm, respectively, ensuring modified absorption.

Z@G (*i.e.*8–10 nm) than pure ZnO (*i.e.* 4–5 nm) as is evident from XRD spectra shown in Fig. 3.

The optical properties of the synthesized ZnO nanoparticles and Z@G nanocomposite samples were also monitored using photoluminescence (PL) spectroscopy as shown in Fig. 6. The PL spectrum of pure ZnO nanoparticles shows a UV emission band centred at 385 nm (3.22 eV), which is related to the recombination of excitons.[46] Moreover, the absence of an emission band in the wavelength range 500–600 nm signifies defect-free, excellent quality ZnO nanoparticles.[47] In comparison, the PL peak position of Z@G nanocomposite shows a red shift to 391 nm (3.17 eV). The shift in the PL emission of Z@G composite might be due to interaction between ZnO nanoparticles and graphene.

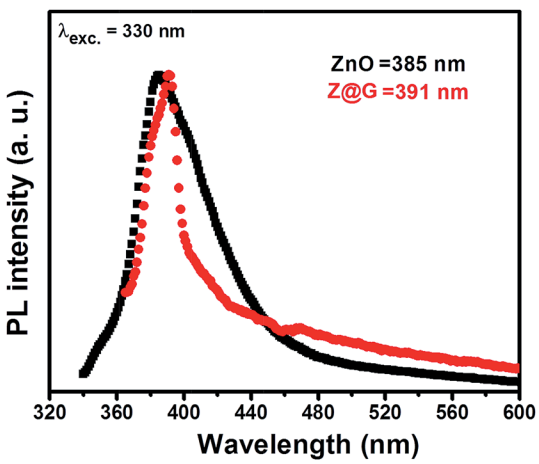

Fig. 6 The normalized PL spectra of synthesized ZnO nanoparticles and Z@G nanocomposite with strong UV emission band peaks at 385 nm and 391 nm, respectively; in response to excitation at 330 nm a red shift is produced that signifies the interaction and coupling between ZnO nanoparticles and graphene.

FTIR and Raman analysis

In order to determine the functional groups attached with ZnO nanoparticles and RGO and also for the identification of chemical changes in RGO because of the anchoring of ZnO nanoparticles (Z@G), Fourier transform infrared (FTIR) spectroscopy was performed (Fig. 7). The broad peak in the range of 3500–3300 cm^{-1} corresponds to the OH stretching vibration in pure ZnO, whereas the peak at 1406 cm^{-1} shows an OH bending vibration. The small peaks at 917 cm^{-1} and 676 cm^{-1} clearly indicates Zn–O stretching,[48] whereas the peaks at 1584 cm^{-1} and 1020 cm^{-1} are attributed to the C–O stretching vibration and unreacted acetate left after the reaction. Now, in the RGO plot, the most intense peak at 1165 cm^{-1} shows the presence of C–O stretching vibration, and the second most intense peak at 1545 cm^{-1} is because of skeletal in-plane vibration of C=C.[49] The peaks in the range 2920 cm^{-1}–2850 cm^{-1} are due to asymmetric C–H stretching; moreover, the small peak positioned at 1736 cm^{-1} can be attributed to stretching vibration for C=O.[50] In the Z@G nanocomposite plot, the intensity of the peak at 1557 cm^{-1} gets maximized, which is due to the skeletal in-plane vibration of C=C, whereas it is less pronounced in RGO data, which is a clear indication of a further reduction of the RGO to graphene. This is further supported by weakened oxygen-related peaks in Z@G nanocomposite at 2365 cm^{-1} and 1013 cm^{-1} than those in RGO, which simply indicates the deoxygenation of RGO toward graphene during the Z@G nanocomposite formation. The peaks at 655 cm^{-1} and 920 cm^{-1} are because of Zn–O stretching, indicating the anchoring of ZnO on the graphene sheet.[48]

Raman spectroscopy being non-destructive is one of the most widely used techniques to investigate order and disorder, specifically in carbon-based materials. The Raman spectra of commercial RGO and hydrothermally synthesized Z@G nanocomposite are shown in Fig. 8. Both samples have the characteristic D-band (1349 and 1353 cm^{-1}) and G-band (1593 and 1597 cm^{-1}); however, the D-band is assigned to local defects and disorders, whereas the G-band originates from the symmetric stretching of sp^2 C–C bond.[51] It can be clearly seen that the D-band of the Z@G nanocomposite is blue-shifted by 4 cm^{-1}, while the G-band is red-shifted by 4 cm^{-1} in comparison to RGO. These shifts indicate the interaction between graphene and ZnO nanoparticles, which is a prerequisite for charge transfer between ZnO and graphene.[52] In addition, the low intensity ratio (I_D/I_G) of D to G-band (0.857 and 0.868) for RGO and Z@G nanocomposite suggests the creation of very few defects in the nanocomposite after the introduction of ZnO nanoparticles.

Hybrid solar cell characterization

In order to develop efficient polymer-based solar cells most of the attention has been paid towards the donor part (*i.e.* conjugated polymers), whereas considerably less work has been performed in the direction of the acceptor part (*i.e.* fullerenes). Some work has been reported by replacing organic fullerenes by inorganic semiconducting acceptors, but results are not considerably significant.[37,40,53] Instead of the total replacement of the organic fullerenes, we have deployed synthesized inorganic nanostructured materials as supplementary acceptors along with organic fullerenes. In this way, we not only exploit the organic blend of polymer:fullerene (PCPDTBT:PCBM) for effective exciton dissociation at the favourable organic–organic interface rather than organic–inorganic interface, but also, at the same time, have the advantage of lowering the overall

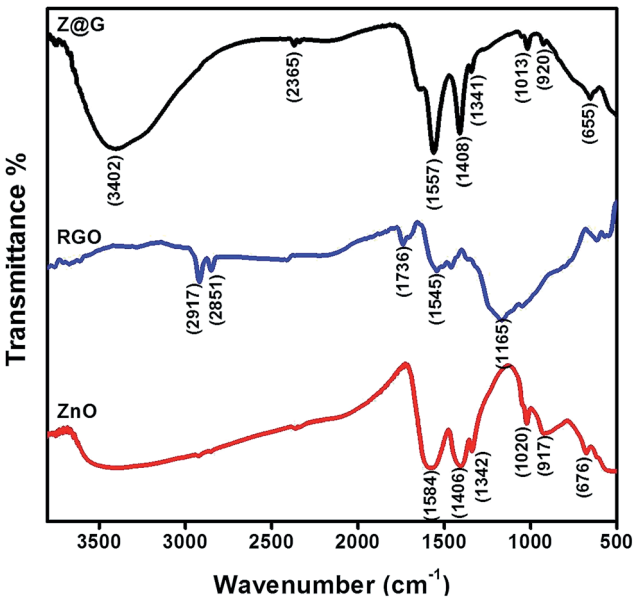

Fig. 7 The FTIR spectra of ZnO nanoparticles, reduced graphene oxide (RGO) and Z@G nanocomposite informing on attached functional groups and chemical changes with anchoring of ZnO nanoparticles at graphene nanosheets.

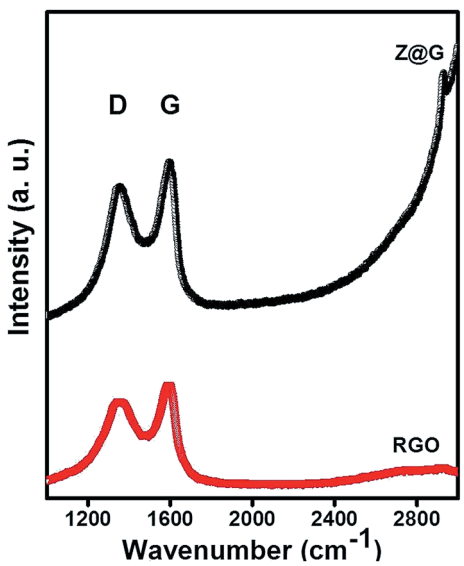

Fig. 8 The Raman spectra of RGO and Z@G nanocomposite shows blue shift (D-band) and red shift (G-band) and low intensity ratio (I_D/I_G), which points out the interaction between ZnO and graphene and the less defective composition of Z@G, respectively.

volume of costly organic blend by supplementing with inexpensive ZnO nanoparticles (or Z@G nanocomposite). Moreover, because of higher charge mobility along with conducting pathways provided by inorganic semiconductors, the charge carriers will get extracted rapidly, which ultimately leads to lower recombination. In this manner, we not only bring down the fabrication cost of polymer-based devices but also achieve better open circuit voltage (V_{OC}) and short circuit current density (J_{SC}) values.

The solar cell devices were fabricated with an overall concentration of 30 mg ml^{-1} and 40 mg ml^{-1} (PCPDTBT:PCBM:ZnO nanoparticles {or Z@G} in chlorobenzene) of active layer and different weight ratios of 1 : 1 : 1 and 1 : 1 : 2 of PCPDTBT:PCBM:ZnO/Z@G, and the corresponding *J–V* characteristics are shown in Fig. 9(a) and (b). All the performance parameters of the solar cells are tabulated in Table 1.

The best efficiency devices (Z-3 and ZG-3) have the weight ratio of 1 : 1 : 1 (PCPDTBT:PCBM:ZnO or Z@G) with an active layer concentration of 40 mg ml^{-1} for both ZnO and Z@G nanocomposite as supplement. When measured under standard AM 1.5 G solar spectrum with a power density of 100 mW cm^{-2}, the best Z@G device gives an efficiency of 3.65% with a J_{SC} value of 17.5 mA cm^{-2}, V_{OC} of 0.66 V and FF of 32%. Similarly, in the case of the ZnO device the best efficiency achieved is 1.76% with J_{SC} of 9.5 mA cm^{-2}, V_{OC} of 0.59 V and FF of 31%.

It is clearly observed that by replacing ZnO nanoparticles by Z@G nanocomposite, the power conversion efficiency of the device becomes more than double with doubling of the J_{SC} value. Note that a small improvement in V_{OC} along with an enhanced J_{SC} value and nearly unchanged FF are observed. The probable reason for increased J_{SC} is the larger specific area of graphene sheets that ultimately leads to large heterojunction interface with polymer matrix for efficient exciton separation, and the ability of graphene to interact with excited ZnO nanoparticles decorated over graphene sheet, followed by the capturing and transportation of charge carriers toward respective electrodes.[24,31,35,45,52] The PL quenching data shown in S4 (ESI†) clearly indicates the charge transfer between the polymer and ZnO nanoparticles (or Z@G nanocomposite).

When the devices are fabricated using Z@G nanocomposite at an overall concentration of 40 mg ml^{-1} but with an increased weight proportion of Z@G, *i.e.* 1 : 1 : 2 (PCPDTBT:PCBM:Z@G) the efficiency gets reduced to 3.18% with the J_{SC} value lowered to 13.6 mA cm^{-2} and a small increment in V_{OC} to 0.71 V (because of the higher content of the wide band gap ZnO, which ultimately affects the open circuit voltage rather than short-circuit current density). The increment in open-circuit voltage is not compensated by the large decrement in short-circuit current density. This is due to the aggregation of Z@G in polymer matrix on increasing the amount of nanocomposite, which will ruin the film homogeneity and ultimately gives rise to a disrupted active layer[54] with inefficient charge transport. In a similar manner, we may explain the decrease in the efficiency of ZnO-based devices on increasing the ZnO nanoparticle content.

Moreover, ZnO and Z@G-based devices (Z-1, ZG-1) prepared with an overall concentration of 30 mg ml^{-1} of active layer give comparatively less efficiency (0.68%, 2.16%) than the devices (Z-3, ZG-3) prepared with a concentration of 40 mg ml^{-1}. The thickness of the active layer may be the probable reason; *i.e.* the thicker the active layer the greater will be the generation of excitons by the enhanced absorption of photons.[55]

From the AFM images shown in Fig. 10(a) and (b), it is very clear that ZnO nanoparticles, owing to their hydrophobic nature, form a very uniform film with PCPDTBT and PCBM, and the low roughness value of 0.325 nm indicates the quality of the active layer for hybrid solar cell device fabrication. The AFM images obtained for ZnO decorated graphene shows some different but interesting patterns in the film. The probable reason for the higher efficiency of the Z@G nanocomposite-based devices may evolve from this uniform pattern. These flake-shaped surface structures may arise due to the hybridization of C-60 compound and graphene sheet as both belong to one or the other form of nanocarbon, and thus, they have no

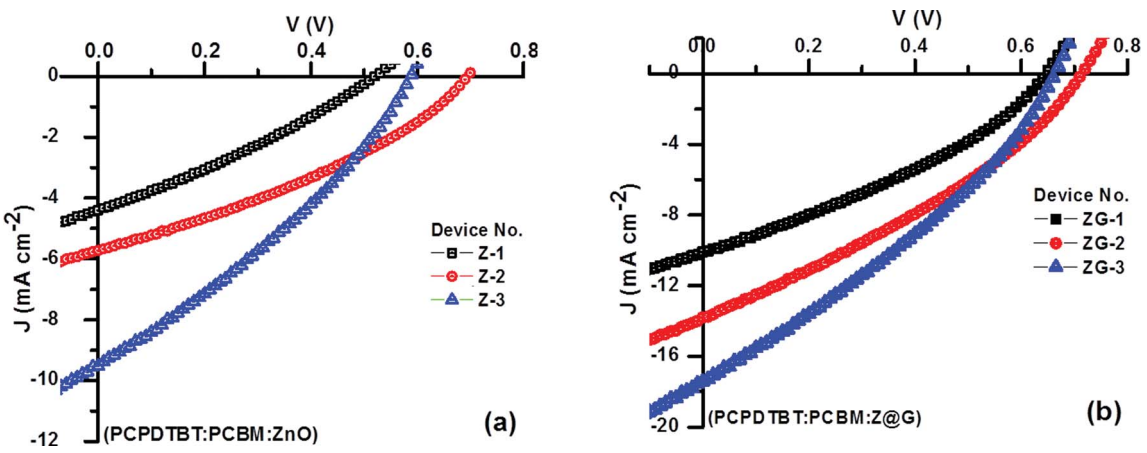

Fig. 9 The *J–V* characteristics of the solar cell devices based on active layer (a) PCPDTBT:PCBM:ZnO nanoparticles {Z-1, Z-2 and Z-3}, and (b) PCPDTBT:PCBM:Z@G nanocomposite {ZG-1, ZG-2 & ZG-3} with overall concentration of 30 and 40 mg ml^{-1} and different weight ratios as 1 : 1 : 1 and 1 : 1 : 2, respectively.

Table 1 Hybrid solar cell performances (ITO/PEDOT:PSS/PCPDTBT:PCBM:ZnO or Z@G/Al) with varied active layer concentration and the weight ratios of organic blend (PCPDTBT:PCBM) and inorganic nanostructures (ZnO or Z@G), respectively

Device architecture		Weight ratio	Device no.	J_{SC} (mA cm^{-2})	V_{OC} (V)	FF (%)	η (%)	R_s (Ω cm^2)	R_{sh} (Ω cm^2)
ITO/PEDOT:PSS/PCPDTBT:PCBM:ZnO/Al	30	1 : 1 : 1	Z-1	4.40	0.52	30	0.68	77	168
	40	1 : 1 : 2	Z-2	5.72	0.69	34	1.34	49	200
	40	1 : 1 : 1	Z-3	9.53	0.59	31	1.76	30	96
ITO/PEDOT:PSS/PCPDTBT:PCBM:Z@G/Al	30	1 : 1 : 1	ZG-1	10.12	0.65	33	2.16	26	107
	40	1 : 1 : 2	ZG-2	13.63	0.71	33	3.18	23	82
	40	1 : 1 : 1	ZG-3	17.45	0.66	32	3.65	18	60

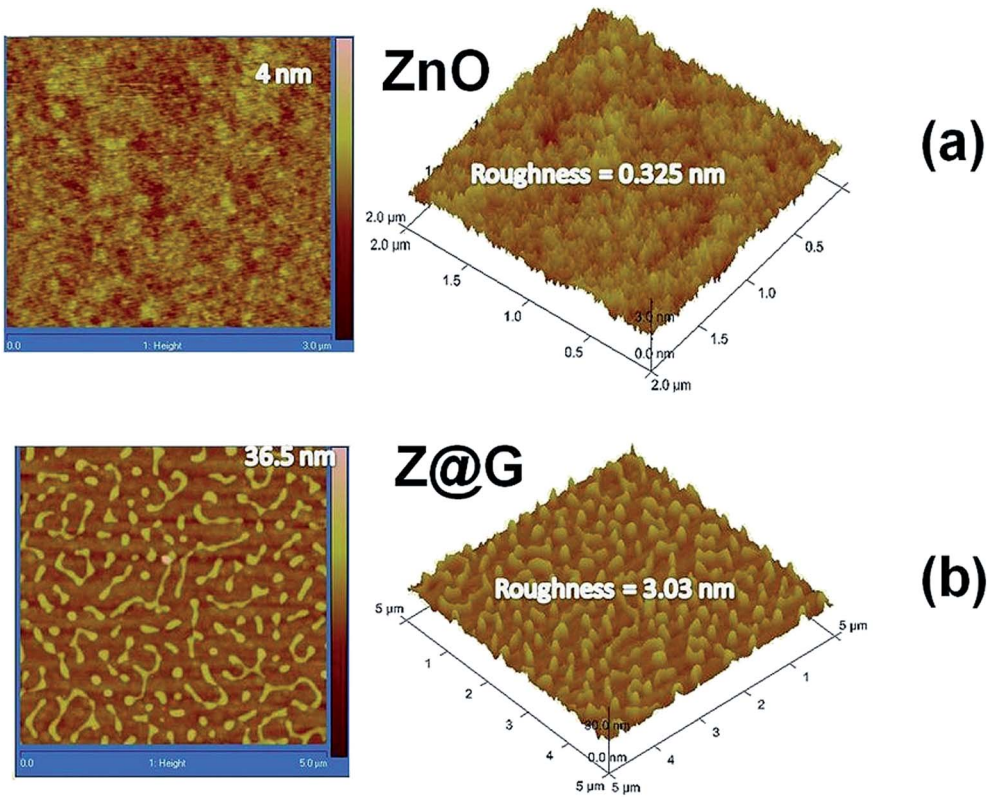

Fig. 10 The AFM micrograph of thin film of (a) PCPDTBT:PCBM:ZnO nanoparticles and (b) PCPDTBT:PCBM:Z@G nanocomposite with roughness 0.32 and 3.03 nm, respectively.

interfacial issues; moreover, the strong affinity between C-60 and carbon allotrope justifies the hybrid formation.[56] Such pattern favours the transportation of charge carriers and thus leads to lower recombination losses and ultimately results in the higher efficiency of the devices.

In order to further probe the nature of enhancement in J_{SC}, the external quantum efficiency (EQE) of cells having ZnO and Z@G has been performed. Fig. 11 represents sharp features in the EQE spectrum of ZnO nanoparticles (or Z@G nanocomposite) blended with PCPDTBT:PCBM. The region centred at 730 nm is dominated by PCPDTBT contribution, while the other one centred at 410 nm can be assigned to ZnO (or Z@G) and PCBM superposition.[57,58] EQE as high as 26% at maximum peak has been achieved in ZnO-based devices, whereas for Z@G, the EQE value jumps to 65%. This is in accordance with the J_{SC} value obtained from J–V curves for ZnO- and Z@G-based devices (Fig. 9). The prominent increase in the EQE for Z@G-based devices demonstrates improved charge transfer that ultimately results in the enhanced short-circuit current density. The densely packed ZnO nanoparticles on graphene sheet generate photoelectrons and have been effectively transferred to graphene. This will suppress the recombination of charge carriers and enhance the transportation of charge carriers toward respective electrodes, which ultimately results in increased short circuit current density.

On comparing the devices made up of the ZnO and Z@G nanocomposite, we clearly observe significant enhancement in short-circuit current (J_{SC}) and thus improvement in overall

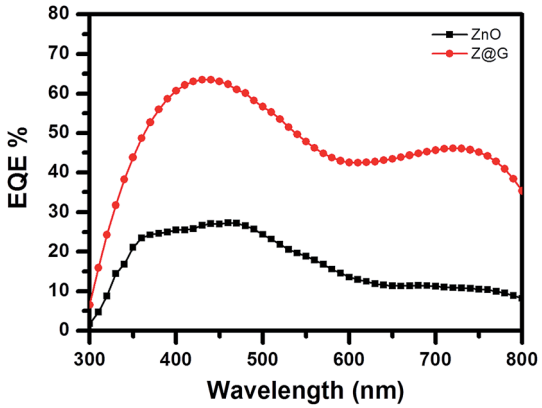

Fig. 11 The external quantum efficiency of PCPDTBT:PCBM:ZnO nanoparticles and PCPDTBT:PCBM:Z@G nanocomposite-based devices, respectively.

efficiency in the Z@G nanocomposite-based devices. However, we need to work on the fabrication of the devices so as to overcome the losses due to series and shunt resistance to obtain better results.

Conclusion

In conclusion, hydrophobic ZnO nanoparticles (ZnO) and ZnO decorated graphene nanocomposite (Z@G) are synthesized *via* a simple and time-efficient microwave-assisted hydrothermal method without using any surfactant. ZnO and Z@G show good solubility in chlorobenzene and thus result in a very smooth and uniform film with polymer and fullerene blend. The power conversion efficiency of PCPDTBT:PCBM:Z@G-based devices show significant enhancement over the PCPDTBT:PCBM:ZnO-based devices. The best performance devices (Z-3 and ZG-3) are obtained at a weight ratio of 1 : 1 : 1 (PCPDTBT:PCBM:ZnO{or Z@G}) with an overall active layer concentration of 40 mg ml^{-1} for both ZnO and Z@G nanocomposite as supplements in polymer-based bulk heterojunction solar cells. The best efficiency achieved in a ZnO-based device is 1.76% with J_{SC} of 9.53 mA cm^{-2}, V_{OC} of 0.59 V and FF of 31%, whereas by replacing ZnO with Z@G the efficiency increases to 3.65% (*i.e.* more than double) with a J_{SC} value of 17.45 mA cm^{-2}, V_{OC} of 0.66 V and FF of 32%. This clearly shows the significant impact of graphene on improved polymer solar cell performance through better charge transportation.

Acknowledgements

The authors would like to thank the Director, National Physical Laboratory, CSIR, New Delhi, for providing materials for the synthesis and their characterization facility. We gratefully acknowledge Indian Institute of Technology Delhi (IITD) for facilitating solar cell device fabrication and characterization. One of the authors, Rajni Sharma, is thankful to CSIR for providing SRF to carry out the research work for the completion of her doctorate.

References

1 F. C. Krebs, *Sol. Energy Mater. Sol. Cells*, 2009, **93**, 394–412.
2 U. Zhokhavets, T. Erb, G. Gobsch, M. Al-Ibrahim and O. Ambacher, *Chem. Phys. Lett.*, 2006, **418**, 347–350.
3 H. Y. Chen, J. Hou, S. Zhang, Y. Liang, G. Yang, Y. Yang, L. Yu, Y. Wu and G. Li, *Nat. Photonics*, 2009, **3**, 649–653.
4 M. A. Green, K. Emery, Y. Hishikawa, W. Warta and E. D. Dunlop, *Prog. Photovoltaics*, 2012, **20**, 12–20.
5 S. H. Park, A. Roy, S. Beaupre, S. Cho, N. Coates, J. S. Moon, D. Moses, M. Leclerc, K. Lee and A. J. Heeger, *Nat. Photonics*, 2009, **3**, 297–302.
6 A. A. Bakulin, A. Rao, V. G. Pavelyev, P. H. M. van Loosdrecht, M. S. Pshenichnikov, D. Niedzialek, J. Cornil, D. Beljonne and R. H. Friend, *Science*, 2012, **335**, 1340–1344.
7 W. Cai, X. Gong and Y. Cao, *Sol. Energy Mater. Sol. Cells*, 2010, **94**, 114–127.
8 S. C. J. Meskers, J. Hubner, M. Oestreich and H. Baessler, *J. Phys. Chem. B*, 2001, **105**, 9139–9149.
9 P. B. Miranda, D. Moses and A. J. Heeger, *Phys. Rev. B: Condens. Matter Mater. Phys.*, 2001, **64**, 812011–812014.
10 T. J. Savenije, J. M. Warman and A. Goossens, *Chem. Phys. Lett.*, 1998, **287**, 148–153.
11 K. M. Coakley and M. D. McGehee, *Chem. Mater.*, 2004, **16**, 4533–4542.
12 S. Gunes, H. Neugebauer and N. S. Sariciftci, *Chem. Rev.*, 2007, **107**, 1324–1338.
13 A. Moliton and J. M. Nunzi, *Polym. Int.*, 2006, **55**, 583–600.
14 B. R. Saunders and M. L. Turner, *Adv. Colloid Interface Sci.*, 2008, **138**, 1–23.
15 M. Skompska, *Synth. Met.*, 2010, **160**, 1–15.
16 Ü. Özgür, Y. I. Alivov, C. Liu, A. Teke, M. A. Reshchikov, S. Doğan, V. Avrutin, S. J. Cho and H. Morkoç, *J. Appl. Physiol.*, 2005, **98**, 041301–041404.
17 S. D. Oosterhout, M. M. Wienk, S. S. van Bavel, R. Thiedmann, L. J. A. Koster, J. Gilot, J. Loos, V. Schmidt and R. A. J. Janssen, *Nat. Mater.*, 2009, **8**, 818–824.
18 S. Shao, K. Zheng, K. Zidek, P. Chabera, T. Pullerits and F. Zhang, *Sol. Energy Mater. Sol. Cells*, 2013, **118**, 43–47.
19 Z. R. Tian, J. A. Voigt, J. Liu, B. Mckenzie, M. J. Mcdermott, M. A. Rodriguez, H. Konishi and H. Xu, *Nat. Mater.*, 2003, **2**, 821–826.
20 S. Shoaee, J. Briscoe, J. R. Durrant and S. Dunn, *Adv. Mater.*, 2013, **26**, 263–268.
21 J. Zhou, N. S. Xu and Z. L. Wang, *Adv. Mater.*, 2006, **18**, 2432–2435.
22 N. M. Gabor, Z. Zhong, K. Bosnick, J. Park and P. L. McEuen, *Science*, 2009, **325**, 1367–1371.
23 B. Farrow and P. V. Kamat, *J. Am. Chem. Soc.*, 2009, **131**, 11124–11131.
24 S. Stankovich, D. A. Dikin, G. H. B. Dommett, K. M. Kohlhaas, E. J. Zimney, E. A. Stach, R. D. Piner, S. T. Nguyen and R. S. Ruoff, *Nature*, 2006, **442**, 282–286.
25 K. I. Bolotin, K. J. Sikes, Z. Jiang, M. Klima, G. Fudenberg, J. Hone, P. Kim and H. L. Stormer, *Solid State Commun.*, 2008, **146**, 351–355.

26 A. A. Balandin, S. Ghosh, W. Bao, I. Calizo, D. Teweldebrhan, F. Miao and C. N. Lau, *Nano Lett.*, 2008, **8**, 902–907.
27 Y. Zhang, T. T. Tang, C. Girit, Z. Hao, M. C. Martin, A. Zettl, M. F. Crommie, Y. R. Shen and F. Wang, *Nature*, 2009, **459**, 820–823.
28 Y. Xu, H. Bai, G. Lu, C. Lu and G. Shi, *J. Am. Chem. Soc.*, 2008, **130**, 5856–5857.
29 Z. F. Liu, Q. Liu, Y. Huang, Y. F. Ma, S. G. Yin, X. Y. Zhang, W. Sun and Y. S. Chen, *Adv. Mater.*, 2008, **20**, 3924–3930.
30 S. W. Tong, N. Mishra, C. L. Su, V. Nalla, W. Wu, W. Ji, J. Zhang, Y. Chan and K. P. Loh, *Adv. Funct. Mater.*, 2014, **24**, 1904–1910.
31 Z. Chen, S. P. Berciaud, C. Nuckolls, T. F. Heinz and L. E. Brus, *ACS Nano*, 2010, **4**, 2964–2968.
32 A. M. Munshi, D. L. Dheeraj, V. T. Fauske, D. C. Kim, A. T. J. van Helvoort, B. O. Fimland and H. Weman, *Nano Lett.*, 2012, **12**, 4570–4576.
33 H. W. Lee, J. Y. Oh, T. Lee, W. S. Jang, Y. B. Yoo, S. S. Chae, J. H. Park, J. M. Myoung, K. M. Song and H. K. Baik, *Appl. Phys. Lett.*, 2013, **102**, 193903.
34 M. Khenfouch, M. Baïtoul and M. Maaza, *Opt. Mater.*, 2012, **34**, 1320–1326.
35 B. Saravanakumar, R. Mohan and S. J. Kim, *Mater. Res. Bull.*, 2013, **48**, 878–883.
36 H. Park, S. Chang, J. Jean, J. J. Cheng, P. T. Araujo, M. Wang, M. G. Bawendi, M. S. Dresselhaus, V. Bulović, J. Kong and S. Gradečak, *Nano Lett.*, 2013, **13**, 233–239.
37 L. Baeten, B. Conings, H. G. Boyen, J. D'Haen, A. Hardy, M. D'Olieslaeger, J. V. Manca and M. K. Van Bael, *Adv. Mater.*, 2011, **23**, 2802–2805.
38 D. E. Motaung, G. F. Malgas, S. S. Ray and C. J. Arendse, *Thin Solid Films*, 2013, **537**, 90–96.
39 Q. Zheng, G. Fang, F. Cheng, H. Lei, W. Wang, P. Qin and H. Zhou, *J. Phys. D: Appl. Phys.*, 2012, **45**, 455103.
40 H. Park, P. R. Brown, V. Buloyic and J. Kong, *Nano Lett.*, 2012, **12**, 133–140.
41 Y. Feng, H. Liu, W. Luo, E. Liu, N. Zhao, K. Yoshino and W. Feng, *Sci. Rep.*, 2013, **3**, 3260.
42 S. Liu, H. Sun, A. Suvorova and S. Wang, *Chem. Eng. J.*, 2013, **229**, 533–539.
43 C. Xu, X. Wang and J. Zhu, *J. Phys. Chem. C*, 2008, **112**, 19841–19845.
44 X. Liu, L. Pan, Q. Zhao, T. Lv, G. Zhu, T. Chen, T. Lu, Z. Sun and C. Sun, *Chem. Eng. J.*, 2012, **183**, 238–243.
45 Y. Yokomizo, S. Krishnamurthy and P. V. Kamat, *Catal. Today*, 2013, **199**, 36–41.
46 J. M. Lee, Y. B. Pyun, J. Yi, J. W. Choung and W. Park, *J. Phys. Chem. C*, 2009, **113**, 19134–19138.
47 H. Park, S. Chang, J. Jean, J. J. Cheng, P. T. Araujo, M. Wang, M. G. Bawendi, M. S. Dresselhaus, V. Bulović, J. Kong and S. Gradečak, *Nano Lett.*, 2013, **13**, 233–239.
48 S. Mitra, P. Patra, S. Chandra, P. Pramanik and A. Goswami, *Appl. Nanosci.*, 2012, **2**, 231–238.
49 F. Jiang, L. W. Yang, Y. Tian, P. Yang, S. W. Hu, K. Huang, X. L. Wei and J. X. Zhong, *Ceram. Int.*, 2014, **40**, 4297–4304.
50 Y. Cao, Z. Lai, J. Feng and P. Wu, *J. Mater. Chem.*, 2011, **21**, 9271–9278.
51 D. Graf, F. Molitor, K. Ensslin, C. Stampfer, A. Jungen, C. Hierold and L. Wirtz, *Nano Lett.*, 2007, **7**, 238–242.
52 H. Yu, T. Wang, B. Wen, M. Lu, Z. Xu, C. Zhu, Y. Chen, X. Xue, C. Sun and M. Cao, *J. Mater. Chem.*, 2012, **22**, 21679–21685.
53 B. R. Saunders, *J. Colloid Interface Sci.*, 2012, **369**, 1–15.
54 W. J. E. Beek, M. M. Wienk and R. A. J. Janssen, *Adv. Mater.*, 2004, **16**, 1009–1013.
55 W. Li, K. H. Hendriks, W. S. C. Roelofs, Y. Kim, M. M. Wienk and R. A. J. Janssen, *Adv. Mater.*, 2013, **25**, 3182–3186.
56 E. K. Jeon, C. S. Yang, Y. Shen, T. Nakanishi, D. S. Jeong, J. J. Kim, K. S. Ahn, K. J. Kong and J. O. Lee, *Nanotechnology*, 2012, **23**, 455202–455208.
57 A. R. Yusoff, H. P. Kim and J. Jang, *Nanoscale*, 2014, **6**, 1537–1544.
58 A. V. Tunc, A. D. Sio, D. Riedel, F. Deschler, E. D. Como, J. Parisi and E. V. Hauff, *Org. Electron.*, 2012, **13**, 290–296.